Weak Crust in Southeast Tibetan Plateau Revealed by Lg-Wave Attenuation Tomography: Implications for Crustal Material Escape

Xi He[1,2] , **Lian-Feng Zhao[1,2]** , **Xiao-Bi Xie[3]**, **Xiaobo Tian[4,5]** , and **Zhen-Xing Yao[1,2]**

[1]Key Laboratory of Earth and Planetary Physics, Institute of Geology and Geophysics, Chinese Academy of Sciences, Beijing, China, [2]Innovation Academy for Earth Sciences, Chinese Academy of Sciences, Beijing, China, [3]Institute of Geophysics and Planetary Physics, University of California, Santa Cruz, Santa Cruz, CA, USA, [4]State Key Laboratory of Lithosphere Evolution, Institute of Geology and Geophysics, Chinese Academy of Sciences, Beijing, China, [5]CAS Center for Excellence in Tibetan Plateau Earth Sciences, Beijing, China

Abstract The continuous convergence between the Indian and Eurasian plates caused massive lithospheric deformation in the Tibetan Plateau and led to excessive crustal material escaping through its southeastern margin. However, the mechanisms that accommodate the escaping materials and whether they intrude into the Indochina Peninsula are continually under debate. Seismic Lg waves mostly propagate within the crust waveguide with an amplitude decay that is sensitive to crustal material properties, such as temperature, partial melting, and fracture. Therefore, Lg attenuation can be a useful indicator of potential crustal material escape. In this study, we developed a high-resolution broadband Lg attenuation model in this region between 0.05 and 10.0 Hz, with the resolution reaching 1° in regions with dense raypath coverage. Prominent low-Q anomalies beneath the southeastern margin of the Tibetan Plateau, correlating with previously observed low velocity, high conductivity and high Poisson's ratio, may indicate possible high temperature and/or partial melting within a relatively weak crust, and suggest a north-south interconnected corridor for gravity-driven material flow. Through our results and other geological and geophysical observations, a dynamic model is suggested here by combining shallow rigid block extrusion and deep viscous crustal flow to explain crustal material escape in the southeastern margin of the Tibetan Plateau. Additionally, neither shallow extrusion nor deep material flow enter the Indochina Peninsula based on the relatively high Q values, which indicate a stronger crust there.

1. Introduction

The continental convergence between the Indian and Eurasian plates that was initiated ∼50 Ma ago led to uplift of the Tibetan Plateau and altered the tectonic framework in Tibetan regions (e.g., Yin & Harrison, 2000). For example, the Indochina Peninsula, situated southeast to the Tibetan Plateau, was suggested to be a consequence of lithospheric extrusion outward from the collision zone due to continental indentation (Huchon et al., 1994; Morley, 2002; Tapponnier et al., 1990). In contrast, the region connecting the southeastern margin of the Tibetan Plateau and the north of the Indochina Peninsula has undergone strong crustal deformation (Royden et al., 2008). Both topographic studies and numerical simulations suggested considerable crustal material loss from the Tibetan Plateau through its margins, especially the southeastern margin (e.g., Clark & Royden, 2000; Royden et al., 1997). Global positioning system (GPS) measurements revealed an eastward flow of crustal material, starting from the interior of the Tibetan Plateau, turning southward around the Eastern Himalaya Syntax and ending with a fan-like front in the southeastern margin (e.g., Gan et al., 2007). However, the mechanisms that accommodate material transfer and crustal deformation in the southeastern plateau are still under debate. The focus is on choosing between the two popular end-member models, the "rigid-block extrusion" model (e.g., Shen et al., 2005; Tapponnier et al., 1990) and the "viscous crustal channel flow" model (e.g., Clark & Royden, 2000), to reasonably explain the growing geological and geophysical observations.

The southeastern margin of the Tibetan Plateau (Figure 1), consisting of southeastern Tibet, the Yunnan Province, and the Western Sichuan Province, is highly fragmented with complicated crustal movements involving both rotation and deformation (X. Xu et al., 2003; P. Z. Zhang, 2013). Several significant strike-slip faults spread over the southeastern margin of the Tibetan Plateau, segmenting the region into dozens
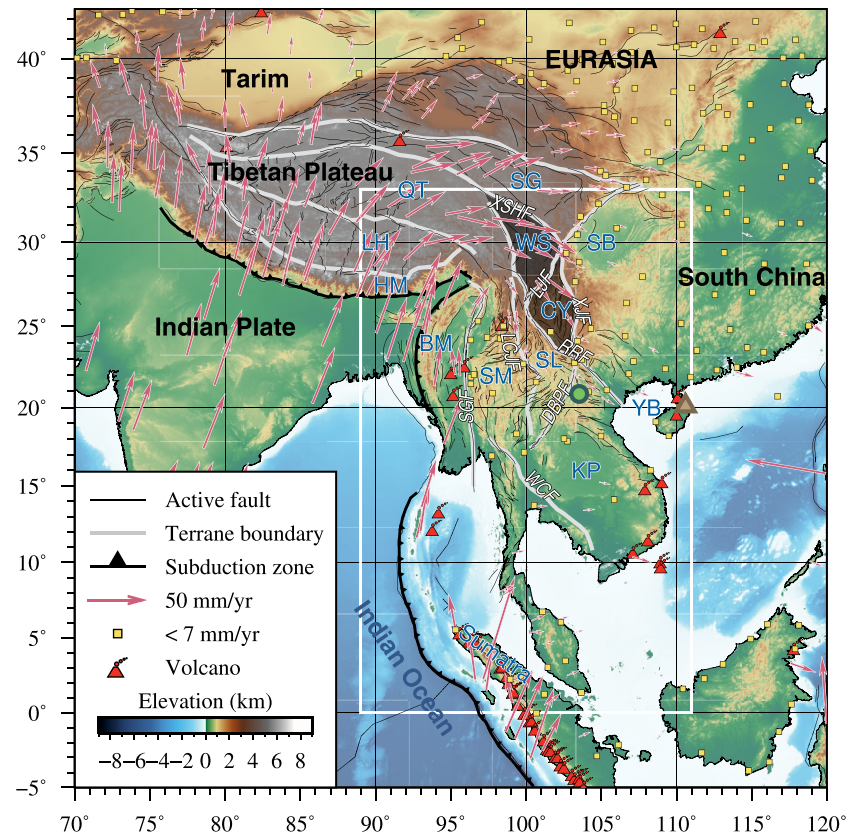
Figure 1. Map showing the Tibetan Plateau including its southeastern margin, and Indochina Peninsula, overlapped with the active faults (thin black lines) and terrane boundaries (light gray lines) with their names labeled (XSHF, Xianshuihe Fault; LJF, Lijiang Fault; XJF, Xiaojiang Fault; LCJF, Lancangjiang Fault; DBPF, Dien Bien Phu Fault; SGF, Sagaing Fault; WCF, Wang Chao Fault), several geological blocks in this region (HM, Himalayan block; LH, Lhasa block; QT, Qiangtang block; SG, Songpan-Ganzi block; SB, Sichuan Basin; WS, Western Sichuan Block; CY, Central Yunnan block; SL, Simao-Lanping block; BM, Myanmar block; SM, Sibumasu block; KP, Khorat Plateau; YB, Yinggehai Basin), and Holocene volcanoes (red volcano signs). The white box outlines the study region in this paper. The green circle and brown triangle denote the location of event 2020/12/30 and station HI.QXL, respectively, and the waveform is shown in Figure 2a as an example. The red arrows and yellow squares denote GPS velocities larger and smaller than 7 mm/yr, respectively (Kreemer et al., 2014). The black shaded area denotes the Chuan-Dian block, which consists of West Sichuan in the northwest and Central Yunnan in the southeast.

of secondary geological blocks (e.g., X. Xu et al., 2003). For example, the northwest-southeast trending Xianshuihe Fault is one of the most active faults in China with a left-lateral slip rate of ~10 mm/yr (e.g., Shen et al., 2005). This left-lateral movement is likely accommodated and absorbed by a series of north-south striking faults in the south, among which the Xiaojiang Fault is the largest one with left-lateral slip of ~7 mm/yr (P. Z. Zhang, 2013; G. Zheng et al., 2017). Additionally, GPS data revealed prominent strain concentrations along the Xianshuihe and Xiaojiang Faults (G. Zheng et al., 2017). These two faults act as the northeastern and eastern boundaries of the Chuan-Dian block, facilitating its southeastward movement and clockwise rotation (P. Z. Zhang et al., 2004). The Chuan-Dian block is further divided by the Lijiang Fault, which has a left-lateral slip rate of ~3 mm/yr, into two inferior blocks, that is, the Western Sichuan block in the northwest and the Central Yunnan block in the southeast (Shen et al., 2005; X. Xu et al., 2003). The crustal strain was concentrated along these geological boundaries and resulted in strong seismic activities (X. Xu et al., 2003; G. Zheng et al., 2017). On the other hand, diffuse deformation occurred in the interior of the Chuan-Dian block (Gan et al., 2007; G. Zheng et al., 2017). Furthermore, many geophysical anomalies, including low velocities, high conductivities, high Poisson's ratios and strong seismic attenuation, were observed, and the observations suggest a weak mid-lower crust in and around the Chuan-Dian block (D. H. Bai et al., 2010, 2015; M. Chen et al., 2014; L. L. Xu et al., 2007; Zhou et al., 2008). Therefore, the crustal flow model may play an important role in understanding material escape through the southeastern margin of

the Tibetan Plateau. Recent studies argued that the two aforementioned models are not irreconcilable (Q. Y. Liu et al., 2014; P. Z. Zhang, 2013). The highly heterogeneous crust and material transfer in the southeastern margin of the Tibetan Plateau could be a consequence of both crustal flow and strain partitioning across faults (Q. Y. Liu et al., 2014; P. Z. Zhang, 2013). However, localized and isolated geophysical anomalies and disordered crustal anisotropy were observed, questioning the pervasive and uniform channel flow of the lower crust (X. Bao et al., 2020; M. Chen et al., 2014; Qiao et al., 2018). In contrast, the Indochina Peninsula was assumed to be relatively stable because of its low elevation and very small crustal deformation, as revealed by GPS observations (Iwakuni et al., 2004; Morley, 2002). Nevertheless, understanding material escape in the southeastern margin of the Tibetan Plateau and its extension is challenging and requires more constraints from high-resolution regional geological and geophysical observations (D. H. Bai et al., 2010, 2015; Zhao, Xie, He, et al., 2013).

The viscoelastic crust exhibits elastic properties that can be described by velocity structures and inelastic behaviors measured by seismic energy dissipation. Seismic attenuation is even more sensitive to thermodynamic related processes in the lithosphere because it is closely related to temperature, partial melting, and fluid and magma movements (Boyd et al., 2004; Sarker & Abers, 1999; Zhu et al., 2013) Therefore, investigating characteristics of attenuations could provide important constraints on the regional tectonics and dynamic evolution.

The Lg-wave is ideal for characterizing the attenuation in the crust. As the reverberated S-wave in the crustal waveguide and the most energetic phase in regional seismograms, it samples the whole crust and is sensitive to variations in crustal properties and fluid contents (e.g., Furumura & Kennett, 1997). Lg waves are intensively attenuated as they pass through tectonically active regions characterized by fault zones, high seismicity and hydrothermal activities. The Lg-wave attenuation can be described by the quality factor Q_{Lg}, with low-Q_{Lg} values denoting strong attenuation and high Q_{Lg} values denoting weak attenuation. Previous studies revealed strong Lg-wave attenuation and significant lateral variations in the southeastern margin of the Tibetan Plateau (e.g., Fan & Lay, 2003). Xie (2002) presented an Lg-wave attenuation model $Q = (129 \pm 9) f^{(0.37 \pm 0.02)}$, with $0.2 \leq f \leq 3.6$, for the eastern Tibetan Plateau, indicating an abnormally high temperature and fluid content in the crust. X. Y. Bao et al. (2012) found low-Q_{Lg} bands in the eastern Tibetan Plateau, which correlated with zones with a low velocity and high strain rate in the middle and lower crust. This correlation suggested that the low-Q_{Lg} bands were attributed to a hot (~700) crust resulting from strain heating along major strike slip fault zones (X. Y. Bao et al., 2012). However, due to the low resolution of previous attenuation measurements, the detailed structures of these low-Q_{Lg} bands and their relationships with regional tectonics remain unresolved. Zhao, Xie, He, et al. (2013) developed a broadband Lg-wave attenuation model for the Tibetan Plateau, suggesting that there is a main crustal flow channel that is characterized by strong Lg attenuation, which turns southeast due to the blockage of the Sichuan Basin characterized by a high Q_{Lg} value. To investigate whether such flow extended through the southeastern margin of the Tibetan Plateau and where it terminates requires further observations in this region and the adjoining Indochina Peninsula.

In this study, we developed a broadband Lg-wave attenuation model for southeast Tibetan Plateau to link the observed low-Q_{Lg} with low temperature and possible partial melting in the crust. Combined with other geophysical and geological data, we further investigated the distributions of potential corridors for crustal materials to escape out of the Tibetan Plateau through its southeastern margin.

2. Data and Methods

This study investigated the frequency-dependent quality factor Q of the crust by measuring the spectral amplitudes of the Lg waves on the vertical component of velocity seismograms. A total of 31,748 vertical seismograms generated by 622 crustal earthquakes that occurred in the southeastern Tibetan Plateau and the Indochina Peninsula between January 1991 and August 2017 were used to construct the Lg wave data set in this study. The seismograms were recorded at 423 seismic stations, including 226 stations from the China Earthquake Network Center (CENC) and 197 stations from the Incorporated Research Institutions for Seismology (IRIS; Figures 4, S1, and Table S1). The focal depths were shallower than the Moho discontinuity from CRUST1.0 (Laske et al., 2013). To improve the signal-to-noise ratios (SNR) and to avoid contamination

from the complex rupture processes of large earthquakes, the earthquake sizes were confined within a magnitude range of $4.1 \leq m_b \leq 6.5$. The very dense station distributions in Southwest China and the large earthquake populations around the Sumatra Islands and the southeastern margin of Tibetan Plateau provided a dense ray coverage over majority of our study region, ensuring a relatively high imaging resolution.

We first estimated the group velocity of the Lg waves in this region. In the vertical-component velocity seismogram (Figure 2a), a remarkable Lg wavetrain arrived at ~220 s with a group velocity of ~3.3 km/s. Various regional phases such as Lg, Pn, Pg, and Sn can also be recognized from the normalized waveform energy (Figure 2b). By aligning normalized waveform energy (square of the ground velocities) according to their epicentral distances (Figure 2c), we can identify various regional phases and estimate their group velocities. The Pg-wave appeared as the first arrival with a group velocity of ~6.0 km/s at shorter distances, while at larger distances, the first arrival was the Pn-wave, whose arrival times generally agreed with those predicted by the IASP91 model (Kennett & Engdahl, 1991). The following phase was the weak Sn wave, which had a group velocity of ~4.5 km/s. We used a basic group velocity window between 3.6 and 3.0 km/s to sample the Lg-waves. To examine this sampling window, we checked all data traces by scanning the waveform energy in the 0.5–5.0 Hz band and in a 0.6 km/s group velocity window shifting between group velocities 3.7 and 2.8 km/s. The results demonstrated that, under most cases, the maximum waveform energy satisfactorily fell within the 3.6 to 3.0 km/s group velocity window used in the calculation. In very limited cases, the maximum energy fell outside the basic sampling window, possibly resulted from the uncertainties in source locations and origin times, or due to complex local geology. For these cases, the Lg sampling windows are slightly adjusted based on the maximum energy arrival (e.g., L. F. Zhao et al., 2010).

Both the pre-event and pre-phase noises were picked before the first *P*-wave arrival and before the Lg phase, respectively, with lengths equal to the Lg-wave group velocity window. The Fourier spectra were calculated for the Lg waves, pre-event and pre-phase noises, and the spectral amplitudes were sampled at 58 discrete frequencies distributed evenly between 0.05 and 10.0 Hz on a logarithmic scale. Next, we calculated SNRs for both pre-event and pre-phase noises at individual frequencies. By setting a pre-event SNR threshold of 2.0, we dropped data with relatively low quality. Furthermore, to ensure that the Lg amplitudes were measured, we also set a pre-phase SNR threshold of 1.0 to remove data that were possibly dominated by Sn coda. These processes significantly reduced the amount of available data at higher frequencies due to strong attenuation of high-frequency signals (Figure S3). Following the processing procedures (L. F. Zhao & Xie, 2016; L. F. Zhao et al., 2010, Zhao, Luo, Liu, & Luo, 2013, Zhao, Xie, He, et al., 2013), noise correction was achieved by applying $A_S^2(f) = A_O^2(f) - A_N^2(f)$, where $A(f)$ is the spectral amplitude and the subscripts S, O and N denote the amplitudes of the true signal, observed data and pre-event noise, respectively. After removing noise, we processed all the regional waveforms to generate the source-station (single-station) amplitudes at individual frequencies:

$$A_{ki} = S_k G_{ki} \Gamma_{ki} P_i R_{ki}, \tag{1}$$

where A_{ki} is the Lg-wave spectral amplitude observed at station *i* for event *k* at a frequency *f*, *S* is the source term, *G* is the geometrical spreading factor, Γ_{ki} is the attenuation term that can be expressed by an integral along a great circle raypath from event *k* to station *i*, *P* is the site response term and *R* is the computational error and cumulative random effects in the Lg propagation between the station *i* and event *k*. The geometrical spreading is $G_{ki} = (\Delta_0 \Delta_{ki})^{1/2}$, with Δ_{ki} representing the epicentral distance from event *k* to station *i* and Δ_0 representing the reference distance fixed at 100 km (Street et al., 1975). When two stations *i* and *j* record the same earthquake *k* and all three are aligned, the source term *S* can be canceled and the inter-station (two-station) amplitude A_{ji} can be obtained by

$$A_{ji} \approx \frac{A_{kj}}{A_{ki}} = \left(\frac{\Delta_{kj}}{\Delta_{ki}}\right)^{1/2} \Gamma_{ji} \left(\frac{P_j}{P_i}\right), \tag{2}$$

where Γ_{ji} represents the contribution from the attenuation between stations *i* and *j*. In addition, a "reference point" approximation is allowed because the geometry of a perfect alignment is not always achievable in practice (L. F. Zhao et al., 2010, Zhao, Xie, Wang, et al., 2013). When station *j* fails to line up with the earthquake *k* and station *i*, a reference point *l* is set on the line between earthquake *k* and station *i*, with its
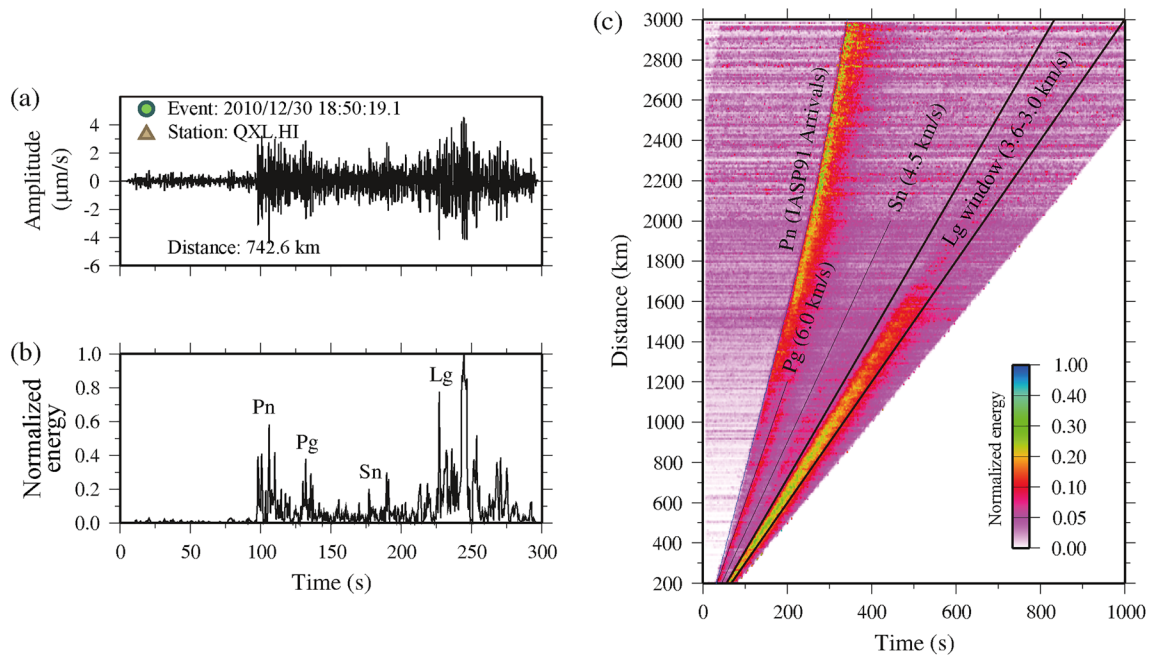
Figure 2. (a) Sample seismogram recorded at station HI.QXL, (b) its normalized energy, and (c) the record section of normalized energy for all data used in this study. The color bar indicates the energy level. The regional phases Pn, Pg, Sn, and Lg are labeled in (b) and (c). Additionally, typical group velocities for these regional phases are indicated in (c).

epicenter distance (Δ_{kl}) equal to that of station j (Δ_{kj}). If the distance between the reference point l and station j is less than half the tomographic grid, we consider the amplitude observed at station j (A_{kj}) as that at the reference point l (A_{kl}), and then, the two-station amplitude A_{lj} can still be obtained by substituting i with l. Taking the case of 1.0 Hz as an example, 43,646 observations were generated, including 22,596 and 21,050 measurements of single-station and two-station Lg-wave amplitudes, respectively. With the single-station amplitudes providing dense data coverage and the two-station amplitudes reducing the trade-off between the source and attenuation, the tomographic scheme made good use of the available data and therefore improved the resolution for Lg-wave Q tomography.

An Lg-wave Q tomography was applied to jointly invert for the regional Q and source excitation based on both the single- and two-station data (L. F. Zhao et al., 2010, Zhao, Xie, He, et al., 2013). This approach has been successfully used to estimate the crustal Lg attenuation in Northeast China (L. F. Zhao et al., 2010), North China (Zhao, Luo, Liu, & Luo, 2013), the Tibetan Plateau (Zhao, Xie, He, et al., 2013), the Middle East (L. F. Zhao & Xie, 2016), the Australian continent (Z. Wei et al., 2017), and eastern North America (L. F. Zhao & Mousavi, 2018). To solve Equations 1 and 2, we calculated Q perturbations and source excitations by using the Least Square QR factorization algorithm (LSQR, Paige & Saunders, 1982). The inversion significantly reduced the root mean square (rms) of the total residuals at all 58 frequencies (Figure S4), suggesting that we can fit the Lg amplitudes using the resulting Q model. Figure 3 shows residual distributions for the initial and final models at 0.5, 1.0, and 2.0 Hz. Note that the rms residuals drops from 1.521, 1.295, and 1.30 to 0.598, 0.674, and 0.842 at 0.5, 1.0, and 2.0 Hz, respectively. The unsolved residuals were then pushed into the site term P. By assuming that the sum of all the changes in the site response $\sum \delta P$ was zero, and that the sum of all the absolute changed in site response $\sum \left| \delta P \right|$ was ε, which is an empirical value for normalizing the site responses, to ensure convergence of site response calculations, we further solved the site response for each station given the inverted source and attenuation (Figures S3a–S3c).

We adopted a checkerboard method to analyze the tomographic resolution based on the current data set. By adding 7% positive/negative perturbations over a constant background Q model to construct the checkerboard model, we synthetized Lg spectral amplitudes based on similar sources, station locations and ray paths as in the real data set. Random noise with an rms perturbation of 7% was added to the synthetic Lg spectra to account for noise. By comparing the Q_{Lg} inverted from the synthetic data with the original
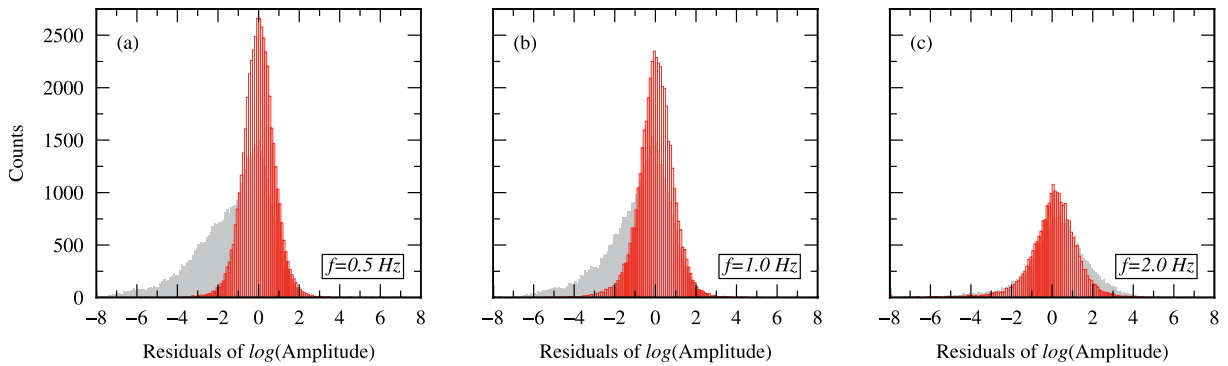
Figure 3. Histograms of the Lg spectral amplitude misfit s before (solid gray) and after (open red) inversions at (a) 0.5, (b) 1.0, and (c) 2.0 Hz.

checkerboard model, the resolutions were investigated. Figure 4 illustrates the raypath coverage and resolution at 1.0 Hz. Dense ray coverage can be seen in the northern part of the study region, while the southeast part is covered by relatively sparse ray paths (Figures 4a–4c). For the southeastern margin of the Tibetan Plateau, the spatial resolution approaches $1° \times 1°$ (Figures 4d–4f).

3. Results

An Lg-wave attenuation model for southeast Tibetan Plateau, including the southeastern margin of the Tibetan Plateau and the Indochina Peninsula, was obtained independently at 58 discrete frequencies by tomographic inversion based on the Lg data set (Figures 5 and 6).

3.1. Q Maps at Individual Frequencies

The Q_{Lg} maps at different frequencies show similar patterns for the large-scale lateral variation, although a general tendency can be recognized where the Q_{Lg} values are higher at higher frequencies than those at lower frequencies (Figure 4). Our resulting Q_{Lg} magnitudes are comparable with the previous results (Ma et al., 2007; Zhou et al., 2008). The lateral Q_{Lg} variations correlate well with the regional tectonics. For example, relatively high Q_0 values (>400), where Q_0 denotes the Q_{Lg} value at 1 Hz, are observed in the Sichuan Basin, where the lithosphere behaves like a craton (Royden et al., 2008). In the Sunda plate, where the GPS velocities revealed a mild intraplate deformation and the receiver functions suggested a crust thickness of ~31 km (L. Bai, Tian, & Ritsema, 2010; Iwakuni et al., 2004), is characterized by relatively high Q_0 values (>300). In contrast, the tectonically active Chuan-Dian and Songpan-Ganzi blocks, which underwent intense deformation, feature low Q_0 values (<200). A similar situation can be seen in the Sumatra Islands, which contain over 30 active volcanoes resulting from the subduction of the Australian plate beneath the Sunda plate. However, we do not observe similar low-Q_{Lg} values for some Holocene volcanoes near the Myanmar volcanic arc, which could be because these volcanoes are associated with relatively small magma chambers that cannot be resolved by the current Lg-wave Q tomography (L. F. Zhao et al., 2010). For instance, located ~200 km east of the Sagaing Fault, the Tengchong Volcano has three magma chambers in the upper crust with horizontal scales of ~19–28 km (C. P. Zhao et al., 2006), and the impact of these magma chambers on the thermal structure is likely inferior to the regional scale and therefore cannot be resolved by the present Lg attenuation model.

3.2. Frequency Cross-Sections of the Lg Attenuation

Frequency cross-sections of Q_{Lg} maps can provide information on Lg attenuation versus both frequency and geological structures (Figure 6). The 30°N profile shown in Figure 6a traverses the eastern Tibetan Plateau and Sichuan Basin, exhibiting a sharp Q_{Lg} variation across the Longmenshan Fault that caused the destructive M_s 8.1 Wenchuan earthquake in 2008 (e.g., W. M. Wang et al., 2008). From the Tibetan side (WS) to the Sichuan side (SB), the dominant attenuation frequency apparently shifted from low to high. Since the frequency dependency of the attenuation is related to the attenuation mechanism, this frequency dependency
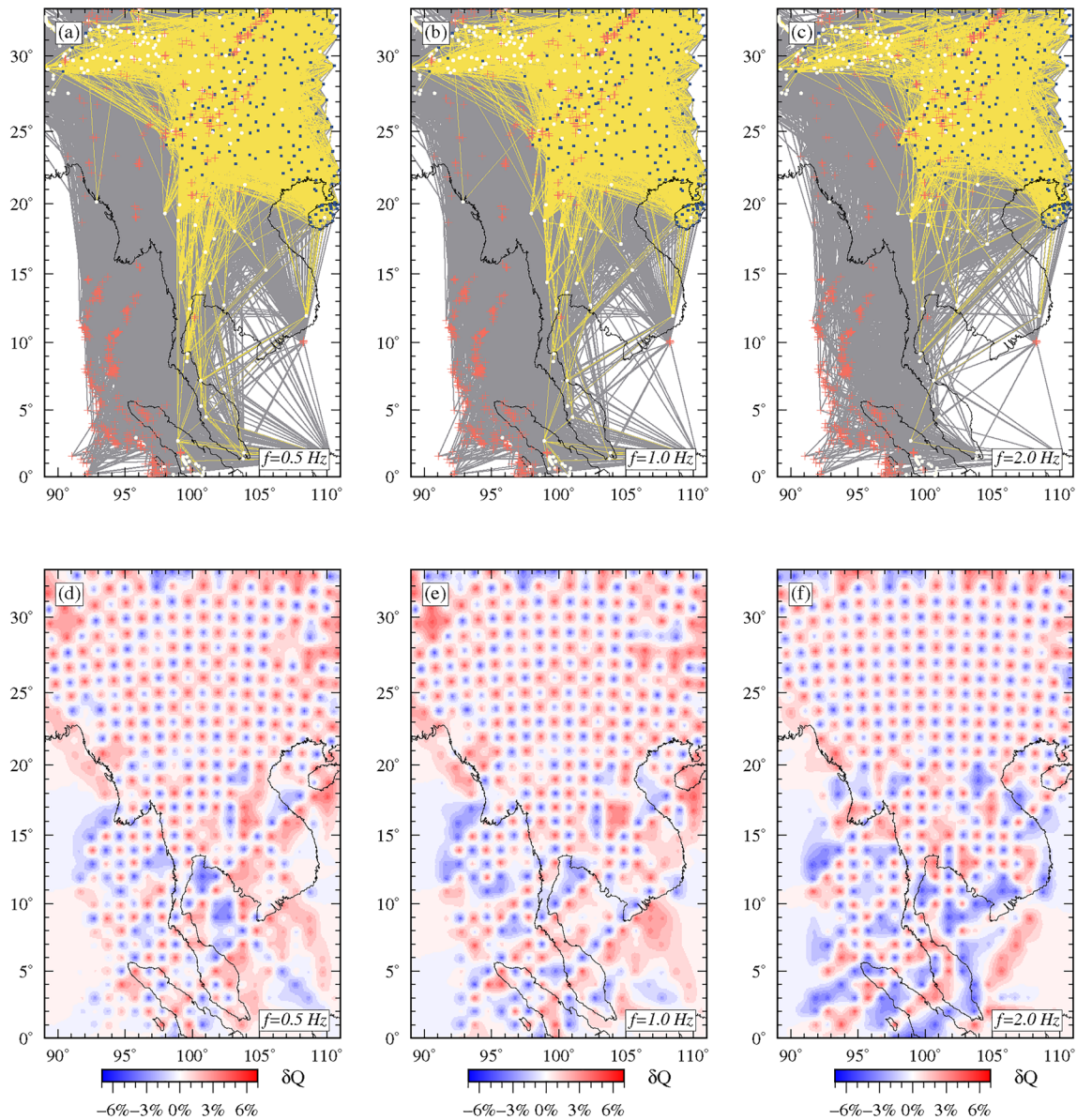
Figure 4. Raypath coverage for (a) 0.5, (b) 1.0, and (c) 2.0 Hz, where ray paths for single and two station data are represented by gray and yellow lines, respectively. The red crosses denote the locations of earthquakes, white and dark blue squares denote CENC and IRIS stations used in this study, respectively; (d)–(f) reconstructed $1.0° \times 1.0°$ checkerboard of Q perturbations at 0.5, 1.0, and 2.0 Hz, respectively.

may provide further information on the underlying processes. In contrast to the relatively high Q_{Lg} beneath the Sichuan Basin, there are two apparent low-Q_{Lg} regions ($Q_{\text{Lg}} < 150$) in eastern Tibet, corresponding to two crustal flow channels in the direction perpendicular to the paper, as suggested by Zhao, Luo, Liu, & Luo (2013). One of these channels extends from northern to eastern Tibet and then turns southeast along the western edge of the rigid Sichuan Basin. This study reveals that the low-Q_{Lg} belt intrudes further south and then gradually breaks into several smaller anomalies beneath the Western Sichuan and Central Yunnan blocks over various frequency ranges (Figure 6b). On this cross-section, slightly higher Q values of ~250 between 0.2 and 0.4 Hz can be seen amidst these low-Q anomalies (as outlined by black lines in Figure 6b), spatially corresponding to a dome structure at the bottom of the crust characterized by high P-wave velocity above 7 km/s (Y. Chen et al., 2015; T. Xu et al., 2015). Previous studies attributed this structure to the Emeishan plume activities during the Permian Period. The localized high Q values may suggest the reduced heat production due to the magmatic underplating of plume activities that replaced the original crust with mafic
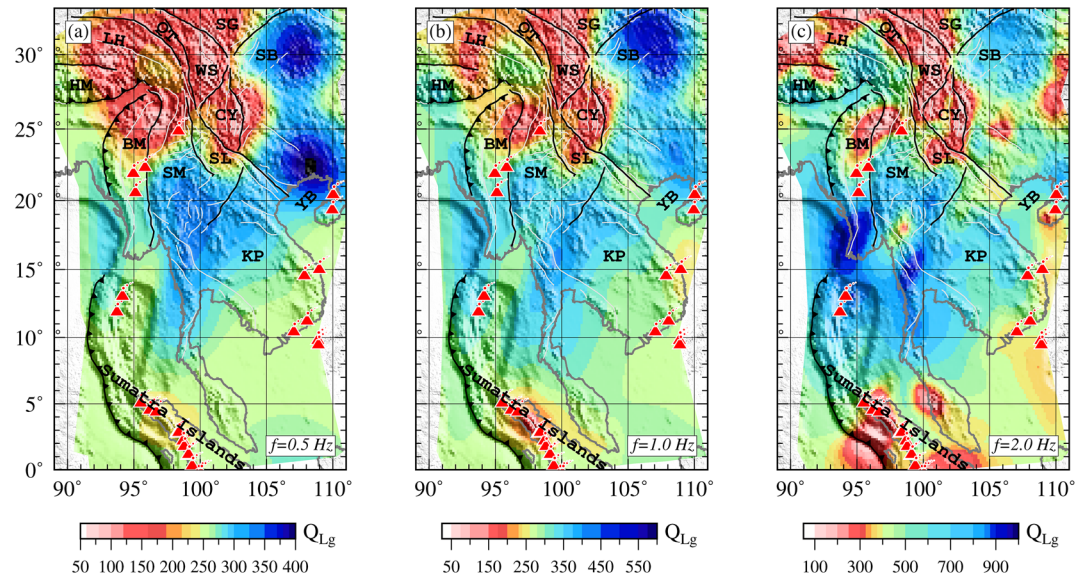
Figure 5. Selected Q_{Lg} maps at (a) 0.5, (b) 1.0, and (c) 2.0 Hz. Abbreviations of geological blocks are labeled in these maps. Additionally, the major faults (black lines), fault systems (gray lines), and locations of Holocene volcanoes (red volcano signs) are denoted. Note that different color scales are used for each Q_{Lg} map.

rocks (Y. Chen et al., 2015). Further south on the 25°N profile, the low Q anomalies between 0.2 and 5.0 Hz appears beneath the Red River Fault and Xiaojiang Fault (Figure 6c), likely to be the southward extension of the low Q anomalies beneath Western Sichuan and Central Yunnan. Low Q values in this frequency range can also be seen beneath the Myanmar block (Figure 6c and 6d), which is likely related to the eastward subduction of the underlying Indian plate (T. Zheng et al., 2020). The Myanmar block and Indian plate have low Q_{Lg} at frequencies of less than ∼0.3 Hz (Figure 6c), and similar cases can also be found for the Sichuan Basin (Figure 6a) and Indian plate (Figure 6b). These areas are characterized by either thick sediments or junctions between the flatland and surrounding mountains, which lead to remarkable scattering of Lg waves (Wu et al., 2007). A relatively high and homogeneous Q_{Lg} is shown on cross-sections that traverse the northern Indochina Peninsula and its central part near the Khorat Plateau (Figure 6e and 6f), suggesting a distinct tectonic intensity from the southeastern margin of the Tibetan Plateau.

3.3. Frequency Dependency of Lg Attenuation

In this study, the broadband Lg-wave attenuation tomography is independently inverted at 58 discrete frequencies, which enables us to investigate the frequency dependency of the Lg-wave attenuation. The frequency dependency varies across geological blocks (Figures 7a–7c). In the frequency band between 0.3 and 2.0 Hz, the behaviors of Q_{Lg} for the three selected blocks follow a similar trend as Q_{Lg} gradually increases with the increase in frequency, although the Q_{Lg} in Chuan-Dian is generally lower and more scattered, which is a reflection of the intensive tectonic activities there. Such a trend can be predicted by the power law relation $Q(f) = Q_0 f^\eta$, where η is the frequency dependency parameter. Based on the linear fitting between the $\log(f)$ and $\log(Q)$, we obtained η for each block at frequency band of 0.3–2.0 Hz. The values of η range from 0.17 to 0.58. However, at frequencies higher than 2.0 Hz, the Q_{Lg} values are strongly dependent on frequency. At frequencies lower than 0.3 Hz, while the Q_{Lg} for Sundaland generally agrees with the continuation of the "power law" over this frequency interval, the Q_{Lg} in the Sichuan Basin and Chuan-Dian block deviates from predictions of the power-law models. The complex frequency dependencies probably indicate various attenuation mechanisms across blocks. The observed Lg-wave attenuation includes both the intrinsic attenuation related to an anelastic process and the scattering attenuation in which the wave energy is scattered from the original propagation direction by small-scale heterogeneities within the crust and at the free surface and Moho discontinuity (Shearer, 2009; Wu et al., 2007). This suggests that interpretations based on the Lg-wave Q at a single frequency can possibly lead to an erroneous estimation because
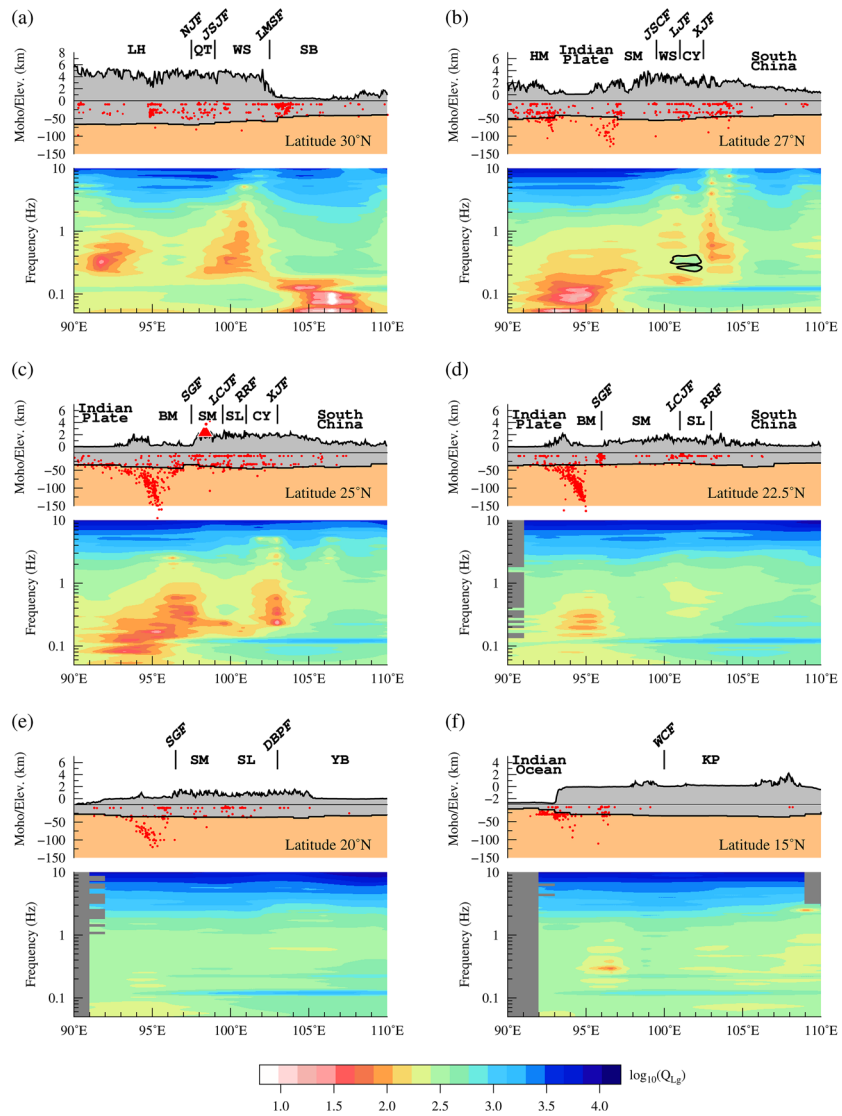
Figure 6. West-east cross-sections at latitudes of (a) 30°N, (b) 27°N, (c) 25°N, (d) 22.5°N, (e) 20°N, and (f) 15°N. For each panel, the topographic elevation, Moho depth, and Q_{Lg} versus frequency are shown from top to bottom. Earthquakes are labeled by red dots with magnitudes greater than 2.5 occurring between 2000 and 2019. Volcano signs in panel (c) indicate Tengchong volcanoes. Codes of geological blocks and major faults are also labeled. The data points in these cross-sections constrained by less than two tomographic rays were painted in gray.

of the particular distribution and size of heterogeneities. For example, seismic scattering within the thick sediments may be a potential cause of the lowest Lg-wave Q at frequencies lower than 0.1 Hz in the Sichuan Basin, where the craton lithospheric structure is expected to result in a relatively high Lg-wave Q, as seen at ~1 Hz. Therefore, to reduce the uncertainty in attenuation mechanism when characterizing the general crustal Lg-wave attenuation, we compare the frequency dependencies for all blocks (Figure 7d), and choose the frequency band of 0.3–2.0 Hz to calculate the broadband average Lg-wave Q (Figure 8 and Table 1). Note that the choice of frequency band may be different among studies because of the distinct scattering attenuation of certain geological blocks involved in individual studies (L. F. Zhao & Mousavi, 2018; L. F. Zhao & Xie, 2016; L. F. Zhao et al., 2010, Zhao, Xie, He, et al., 2013, Zhao, Xie, Wang, et al., 2013).
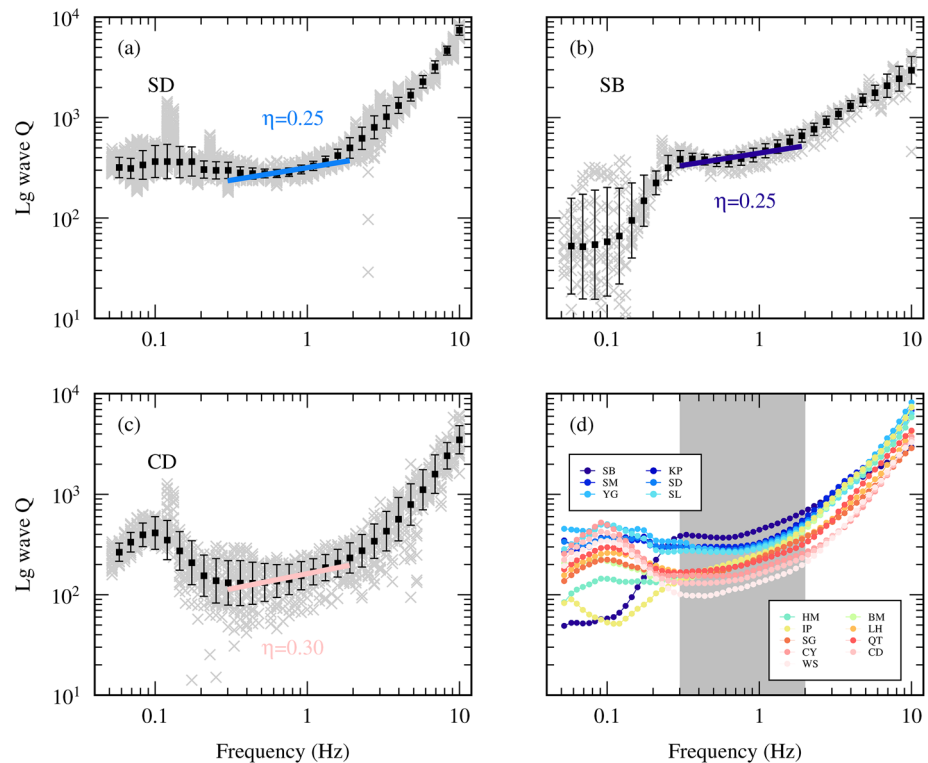
Figure 7. Selected frequency-dependent Q for (a) Sundaland, (b) Sichuan Basin, and (c) Chuan-Dian block. The directly inverted Q values (gray crosses) are plotted for individual blocks, along with their values averaged within narrow frequency bands (black squares) and their logarithmic standard deviations (error bars). The band-limited power-law models are obtained within 0.3–2.0 Hz, and are denoted by colored lines with their frequency dependence parameters η labeled. (d) Comparison of the average Q values of individual blocks. The shaded area highlights the 0.3–2.0 Hz frequency band, within which all Lg-wave Q vary in a similar trend.

4. Discussion

4.1. Weak Crust in the Southeastern Margin of the Tibetan Plateau

Our Lg-wave attenuation model reveals a zone of significantly strong Lg attenuation with a broadband Q_{Lg} value lower than 200 that extends southeastward from Songpan-Ganzi and Western Sichuan to Central Yunnan (Figure 8). These regions are characterized by intense crustal deformation, intricate fault systems, and rough topography, which may result in remarkable Lg-wave scattering and contribute to the low-Q_{Lg} anomalies observed near major faults, including the Xianshuihe, Xiaojiang, Lijiang, and Sagaing faults (Wu et al., 2007). However, many studies have reported anomalies of high Poisson's ratio, low S-wave velocity, and high conductivity within the crust in these regions (D. H. Bai et al., 2010; X. Bao et al., 2020; X. W. Bao et al., 2015; H. P. Chen et al., 2016; M. Chen et al., 2014; Q. Y. Liu et al., 2014; Qiao et al., 2018; Sun et al., 2012, 2014; W. L. Wang et al., 2017). The strong Lg attenuation obtained in this study also coincides with these anomalies, which seems to indicate that the intrinsic attenuation associated with thermal status and partial melting is an important origin of the Lg-wave dissipation, in addition to the scattering effects.

Receiver function studies suggested relatively high Poisson's ratio that exceeds 0.28 (corresponding to a V_P / V_S ratio higher than ~1.8) beneath the southeastern margin of Tibetan Plateau (Sun et al., 2012; W. L. Wang et al., 2017). L. L. Xu et al. (2007) suggested that the widely observed intracrustal low-velocity zones (~12%–19% reduction in S-wave velocity) may become thinner toward the southeast beneath part of Songpan-Ganzi, Western Sichuan, and Central Yunnan. The intracrustal low-velocity zones together with a Poisson's ratio of 0.30 or higher suggested the presence of the partial melting beneath the southeastern Tibetan Plateau (e.g., Owens & Zandt, 1997). Nevertheless, the partial melting is not widespread; instead, it is more likely to be confined within narrow areas (D. H. Bai et al., 2010; X. W. Bao et al., 2015). Joint analysis of the receiver functions and Rayleigh-wave dispersion revealed two channels with a low S-wave velocity in the
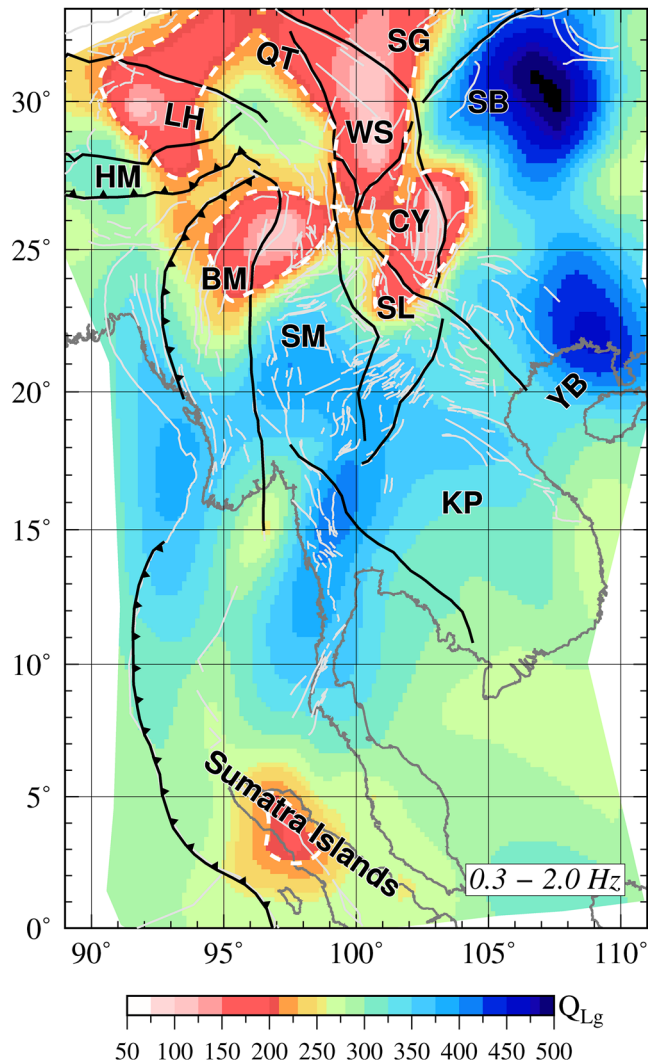
Figure 8. Broadband Lg attenuation obtained by averaging the Q_{Lg} values within the frequency range of 0.3–2.0 Hz (shaded area in Figure 6d). The contour of $Q_{Lg} = 220$ is indicated by the thick white dot-dashed line. For abbreviations see the caption of Figure 1.

mid-lower crust for the Chuan-Dian block, seemingly bending around the East Himalayan Syntax (X. W. Bao et al., 2015). Magnetotelluric images revealed that there are two channels of high electrical conductivity located at depths of 20–40 km that extend horizontally over 800 km from southeastern Tibet into southwestern China, implying abundant fluid contents of 5%–20% (D. H. Bai et al., 2010). Moreover, the southeastern margin of the Tibetan Plateau exhibits crust-induced high heat flow (Jiang et al., 2019). Therefore, the strong Lg attenuation beneath the Chuan-Dian block, which is generally well correlated with the aforementioned geophysical anomalies, could be attributed to partial melting and a weak crust. There are two mechanisms that can cause such strong Lg attenuation beneath the Chuan-Dian block, either intrinsic or scattering attenuation. The intrinsic attenuation can result from the partial melting and high-temperature properties of deep crust materials, and the scattering attenuation can be a consequence of complex structures of the upper crust. However, it is difficult to distinguish between the two attenuation mechanisms based on the methods used and limited observations. Therefore, we combine the observed strong apparent Lg attenuation with other geophysical anomalies, including low seismic velocities, high conductivities, high Poisson's ratio and high heat flow, to provide constraints on the distribution and location of high temperature and partial melting, hence inferring a corridor of possible crustal material flow. Thanks to better data coverage, the broadband Lg attenuation model obtained in this study suggests that the weak crust beneath Chuan-Dian was related to the low-Q_{Lg} anomalies beneath Songpan-Ganzi in the north, and in the south, the low-Q_{Lg} zone does not extrude into the Indochina Peninsula interior, although it extended beyond the Red-River Fault.

4.2. Crustal Flow Beneath the Chuan-Dian Block

The presence of partial melting can dramatically reduce the viscosity and rheological strength of the crust. The mechanically weakened crust may behave like fluid and flow over a geological time scale due to the gravitational potential and/or gradient of tectonic stress, which accommodates lateral growth of the Tibetan Plateau (Beaumont et al., 2004; L. Chen et al., 2019; Jamieson et al., 2011). The abrupt change in Q_{Lg} values across the Longmenshan Fault may reflect the contrast in crustal strength between the Songpan-Ganzi block and Sichuan Basin (Figures 6a and 9a). This finding supports the crustal flow model for accommodating the eastward expansion of the plateau. The crustal material flow was blocked by the mechanically strong Sichuan Basin. Therefore, the crust piles up, thickens, and hence leads to plateau build-up and crustal thickening without sufficient Neogene shortening in eastern Tibet (e.g., Clark & Royden, 2000; Royden et al., 2008; P. Z. Zhang, 2013). In the Chuan-Dian and Songpan-Ganzi blocks, the pattern of low-Q_{Lg} zones is correlated well with the clockwise movement and rotation of the geological blocks revealed by GPS measurements, which indicates that the crustal material flow turns south into the Chuan-Dian block (Figures 8 and 9d). The 2,000 m elevation contour and 45 km crust thickness contour are added to Figure 9a, to compare with regional Lg-wave Q. The high elevation and thick crust protrude outward from the Tibetan Plateau, consistent with the southward extension of the low-Q anomalies beneath the Chuan-Dian block. The epicenters of earthquakes with magnitudes greater than 5.5 are also included in Figure 9a. The elevation of the northern Chuan-Dian block is higher than its southern part by ∼2,000 m (from 4,000 m down to 2,000 m) Accordingly, the gravitational potential could drive crustal material flow. GPS data suggested a significant dilatational strain of ∼7 nanostrain/yr and southeastward surface motion of ∼18 mm/yr in the Chuan-Dian block (P. Z. Zhang et al., 2004; G. Zheng et al., 2017). This may be related to the underlying material flow of the relatively weak lower crust based on the strong Lg attenuation

Table 1
Lg-Wave Q for Individual Geological Blocks

Geological block	Abbreviation	Q_0 1 Hz	Broadband Q 0.3–2.0 Hz	Frequency dependence η 0.3–2.0 Hz	Crustal thickness[a] (km)	Sediment thickness[a] (km)
Sichuan Basin	SB	444 (410–481)	476 (433–522)	0.24 ± 0.07	42.7 ± 2.8	7.1 ± 1.3
Khorat Plateau	KB	329 (318–340)	363 (337–390)	0.27 ± 0.07	35.1 ± 0.8	2.6 ± 1.7
Sibumasu block	SM	325 (297–355)	360 (319–407)	0.21 ± 0.05	35.5 ± 3.1	0.1 ± 0.1
Sunda plate	SD	318 (301–335)	345 (318–375)	0.25 ± 0.03	34.8 ± 2.1	0.8 ± 1.3
Yinggehai Basin	YG	306 (295–317)	335 (309–363)	0.16 ± 0.12	32.4 ± 0.5	3.9 ± 2.3
Simao-Lanping block	SL	293 (259–332)	319 (277–368)	0.20 ± 0.07	36.7 ± 4.4	0.1 ± 0.1
Himalayan block	HM	255 (233–281)	267 (233–306)	0.56 ± 0.07	56.5 ± 8.2	0.0 ± 0.1
Myanmar block	BM	253 (220–292)	256 (207–317)	0.58 ± 0.04	37.1 ± 5.0	3.9 ± 3.2
Indian plate	IP	252 (241–264)	269 (251–288)	0.52 ± 0.07	41.4 ± 3.5	1.4 ± 1.6
Lhasa block	LH	238 (221–256)	244 (205–292)	0.47 ± 0.04	68.5 ± 5.4	0.0 ± 0.0
Songpan-Ganzi block	SG	234 (190–287)	242 (196–298)	0.51 ± 0.06	60.6 ± 7.3	0.0 ± 0.0
Qiangtang block	QT	219 (208–231)	227 (205–250)	0.32 ± 0.05	70.1 ± 2.9	0.0 ± 0.0
Central Yunnan block	CY	182 (162–205)	192 (161–230)	0.25 ± 0.07	46.1 ± 4.9	0.5 ± 0.7
Sichuan-Yunnan block	CD	162 (139–189)	169 (139–206)	0.30 ± 0.05	54.1 ± 8.1	0.2 ± 0.5
Western Sichuan block	WS	134 (115–156)	137 (115–162)	0.40 ± 0.06	60.8 ± 3.3	0.0 ± 0.0

[a]From CRUST1.0 (Laske et al., 2013).

observed in this region. The lower crustal flow could result in strong crustal anisotropy, decoupling of the crust from the underlying mantle to some degree, and facilitate the motions of the brittle upper crustal blocks (Sun et al., 2012). Isotope paleoaltimetry for several sedimentary basins revealed that Western Sichuan was near its current elevation by the Eocene, preceding the late Miocene surface uplift in the southern part of Central Yunnan (Hoke et al., 2014; Li et al., 2015). The surface uplift seems to result from crustal thickening due to the southward extending of the lower crustal material flow. For the southernmost part of the Central Yunnan block, where low Lg-wave Q and low S-wave velocity are observed without high Poisson's ratio, we attribute the discrepancy to southeastern-ward thinning intracrustal low velocity zones (L. L. Xu et al., 2007), which result in a decrease of the thickness of the lower crust and thus an increasing felsic component in the crust. However, the strong attenuation and reduced *S*-wave velocity could still suggest a strength reduction within the crust.

4.3. Does the Emeishan Large Igneous Province Block the Lower Crustal Material Flow?

The Emeishan Large Igneous Province (ELIP; Figure 9a), located in the southeastern margin of the Tibetan Plateau, features voluminous volcanic sequences that erupted in a short period of time, which result in significant accumulations of extrusive and intrusive mafic materials (e.g., Richards et al., 1989). The inner ELIP is bounded by the Red River Fault to the southwest, the Xiaojiang Fault to the east, and the Lijiang Fault to the northwest (He et al., 2003), where mafic emplacements in the crust were indicated by high P-wave velocity (Y. Chen et al., 2015; Z. Liu et al., 2017; T. Xu et al., 2015). Rayleigh-wave tomography and receiver function studies revealed that the S-wave velocities were relatively high in the inner ELIP, whereas lower velocities observed beneath the Central Yunnan block were disconnected from those beneath the Western Sichuan and Songpan-Ganzi blocks (X. W. Bao et al., 2015; H. P. Chen et al., 2016; Qiao et al., 2018). These observations contradicted the model of a pervasive and uniform lower crustal channel flow.

However, interpretations based solely on the seismic velocities are more likely limited by uncertainties in the origin of the anomalies because seismic velocity is sensitive to both temperature and composition and could be elevated by increasing temperature and reduced by increasing mafic material accumulated during basalt floods. The seismic attenuation is more sensitive to temperature and less affected by composition
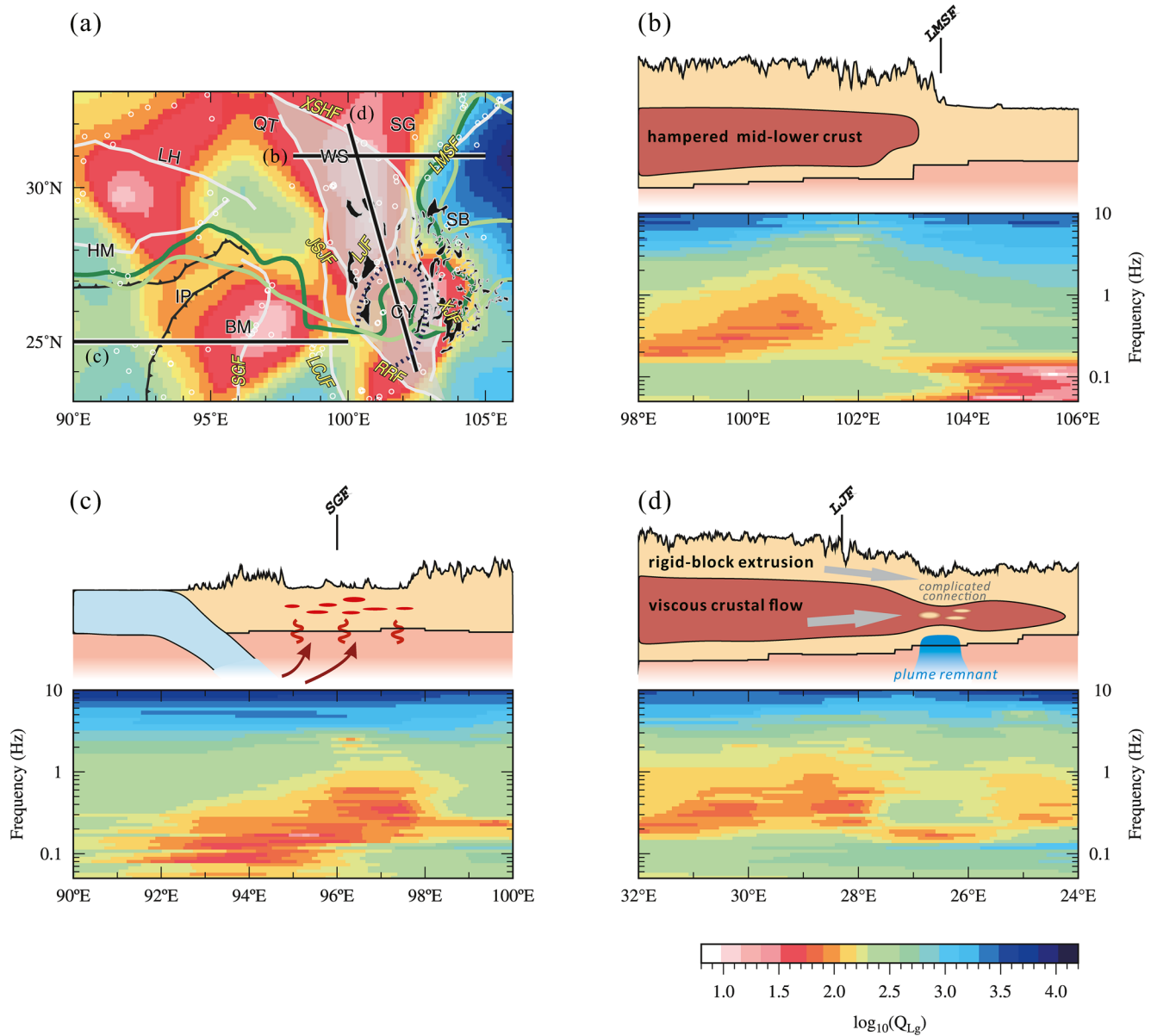
Figure 9. (a) Zoomed-in view of the broadband Q_{Lg} map for the southeastern margin of the Tibetan Plateau with three profiles, along which the Q_{Lg} and schematic diagram of the inferred tectonic model are shown in (b), (d), and (c), respectively. The color scale for (a) is the same as that in Figure 8. The dark blue dashed line and black areas in (a) represent the inner zone of the Emeishan Large Igneous Province and the Emeishan basalts, respectively (Y. Chen et al., 2015). Locations of earthquakes with magnitude M_S greater than 5.5 are denoted by white open circles. The dark and light green lines represent the contour of topographic elevation of 2,000 m and contour of crustal thickness of 45 km. Descriptions of profiles are provided in the text.

variations (e.g., Boyd et al., 2004; Sarker & Abers, 1999). Thus, crustal Lg attenuation may provide significant constraints on whether the ELIP blocked the crustal material flow. In this study, based on the denser data coverage, we can construct an Lg attenuation model with a high resolution in the Chuan-Dian region than that in a previous study (Zhao, Xie, He, et al., 2013), and the new model is expected to identify small branches of crustal flow channels. Figure 9a shows the Q_{Lg} map between 0.2 and 3.0 Hz, which demonstrates interconnected anomalies of strong Lg attenuation beneath the Chuan-Dian block, although the inner ELIP in the middle Chuan-Dian block is characterized by the slightly higher Q_{Lg} values. In Figure 9d and 9a southeastward frequency cross-section along the trend of low-Q_{Lg} zones beneath the Chuan-Dian block is illustrated, which shows low-Q_{Lg} anomalies beneath the inner ELIP at various frequencies. These results suggest that low-Q_{Lg} anomalies are connected in spite of strong inhomogeneity, probably indicating

complicated connections for crustal material flow. The inhomogeneous crustal flow was also suggested by seismic anisotropy investigations (X. Bao et al., 2020; H. Huang et al., 2010, Z. C. Huang et al., 2015; W. Wei et al., 2013). W. Wei et al. (2013) observed remarkable low velocity zones beneath Songpan-Ganzi and Chuan-Dian at depths of 20–40 km but a disordered anisotropy with inconsistent directions of fast velocity with low-velocity zone trends (W. Wei et al., 2013). The disordered pattern of the fast velocity direction probably reflects the nature of the complicated connections within the corridor of lower crustal material flow because the occurrence of lower crustal flow would result in the strain-induced lattice-preferred orientation of minerals at these depths (X. Bao et al., 2020). By simulating shear-wave splitting based on a 3-D anisotropic S-wave velocity model from Rayleigh surface-wave tomography, Yao et al. (2010) suggested that ductile deformation occurred in low-velocity zones in the deep crust and favored crustal material flow, with a complicated pattern indicated by lateral variations in both velocity and anisotropy. However, to the south of Central Yunnan, the fast directions of SKS splitting change abruptly from nearly N-S to nearly E-W with the maximum extension under N-S shortening in the crust, which suggests that the crust and mantle may be coupled and that there is no lower crustal flow in this area (Z. C. Huang et al., 2015). This result is consistent with the relatively high Q_{Lg} observed in this study and therefore, the crustal flow does not extend into the Indochina Peninsula.

4.4. Asthenosphere Upwelling Beneath Northern Myanmar

In northern Myanmar, strong Lg attenuation with broadband Q less than ~200 is also revealed, overlying the eastward subduction of the Indian plate. The subduction of the Indian plate involves not only the northward subduction beneath the Tibetan Plateau but also the eastward component beneath the Myanmar arc (T. Zheng et al., 2020). Its Wadati-Benioff zone can be delineated by the seismicity down to ~150 km (Stork et al., 2008). Numerous teleseismic tomography studies have revealed the eastward-dipping anomalies with high seismic velocities, which could be interpreted as the subducting Indian lithosphere (Z. C. Huang et al., 2015; Lei & Zhao, 2016). In addition, low Q values in northern Myanmar are accompanied by the reduced P-wave velocity of less than ~7.9 km/s in the uppermost mantle (e.g., Lv et al., 2017), suggesting that the strong attenuation within the crust may be related to the underlying subduction processes. The discontinuity of the subducting slab and variation in the dipping angle have led to speculation of slab tearing between the continental Indian plate and preceding Neo-Tethys oceanic slab (Pesicek et al., 2010). The resultant slab window probably triggered the upwelling of hot mantle material, which is consistent with the observed depressed 410-discontinuity (e.g., Xu et al., 2018) and coeval igneous activities (J.-H. Wang et al., 2001; Yu et al., 2017). Therefore, the strong Lg attenuation in northern Myanmar may indicate a hot and/or fluid-rich crust due to the upwelling of hot asthenosphere. Moreover, a local regime of extensional stress, near northern Myanmar and within the range of low Q anomaly here, was revealed by the regional stress field inverted from GPS measurements and focal mechanisms of crustal earthquakes, which could also be associated with the upwelling (K. L. Zhang et al., 2019; Zhao, Luo, Liu, & Luo, 2013). By comparing to Western Himalayan Syntax, where the subduction occurred in the absence of upper crust, T. Zheng et al. (2020) suggested that the eastward subduction of the entire Indian continental crust was the consequence of both oblique collision and sideway extrusion. Analogously, the eastward subduction of Indian plate also plays an important role to the crustal deformation in the southeast Tibet Plateau, because the subsequent processes related to the subduction, including asthenosphere upwelling and slab retreating, could resulted in the weakened crust and extensional stress, probably decreasing the resistance to the escape of crustal material in the southeastern margin of Tibetan Plateau.

In summary, the resultant Q_{Lg} model, along with other observations, such as seismic velocity structure, electrical structure, crustal Poisson's ratio, seismic anisotropy, GPS velocity, fault kinematic and paleoelevation reconstruction, suggests a combination model for a viscous crustal flow in the mid-lower crust and a rigid block extrusion in the brittle upper crust that accommodates crustal deformation and seismic activities in the southeastern margin of the Tibetan Plateau (Figure 9b and 9d). The crustal component, which was modified by the Permian plume activities in the inner ELIP, resulted in a complicated interconnection within the corridors of the crustal flow, rather than truncating the flow (Figure 8d). The strong Lg attenuation observed in northern Myanmar may result from the eastward subduction of the Indian plate because the associated upwelling of the hot mantle material increased the temperature within the crust (Figure 9c).

This process also plays an additional important role in the crustal deformation of the southeastern margin of the Tibetan Plateau, as its resulting extensional environment creates space for escaping crustal material.

5. Conclusion

We developed a broadband Lg-wave attenuation model for southeast Tibetan Plateau, including the southeastern margin of the Tibetan Plateau and the Indochina Peninsula. The frequencies are between 0.05 and 10.0 Hz and the resolution approaches ~1°. The regional variations in Lg attenuation generally correlate with geological blocks with different tectonic activities. Strong Lg attenuation is observed beneath the Chuan-Dian block. By simultaneously considering low Q_{Lg}, high crustal Poisson's ratio, low velocity and high conductivity at depths ranging from 20 to 40 km, we suggest that the partial melting may occur in the mid-lower crust, leading to a gravity-driven flow of the rheologically weak lower crust. Therefore, the crustal deformation in the southeastern margin of the Tibetan Plateau involves lower-crustal flow and tectonic southeastward movements of the upper crust. A relatively weak and complicated connectivity for the crustal material flow was revealed by our Lg attenuation model. The ELIP partly blocks the flow of massive crustal materials but does not entirely truncate the flow. In contrast, the Indochina Peninsula is characterized by relatively high Q_{Lg} values, an ~30 km crustal thickness and mild interior deformation, exhibiting distinct tectonics from the southeastern margin of the Tibetan Plateau. Therefore, the crustal materials do not escape into the Indochina Peninsula. Both strong Lg attenuation in the crust and low Pn velocity in the upper mantle are observed in the northern Myanmar block, suggesting the ongoing eastward subduction of the Indian plate, which results in asthenospheric upwelling and a hot and fluid-rich crust in this region. Such a mantle upwelling occurred in an extensional environment that creates space for crustal material to move out of the Tibetan Plateau through its southeastern margin. Therefore, in addition to the incorporated model involving both "rigid block extrusion" and "viscous crustal flow," the eastward subduction beneath Myanmar is also important in understanding the crustal deformation of the southeastern margin of the Tibetan Plateau.

Data Availability Statement

The waveforms used in this research were collected from the China Earthquake Network Center (CENC), the Data Management Center of China National Seismic Network at the Institute of Geophysics, the China Earthquake Administration, and the Incorporated Institutions for Seismology Data Management Center (IRIS DMC). The single- and two-station Lg amplitude data used in this study can be accessed from WDC for Geophysics, Beijing (http://www.geophys.ac.cn/ArticleDataInfo.asp?MetaId=301, DOI: 10.12197/2021GA002).

References

Bai, D. H., Unsworth, M. J., Meju, M. A., Ma, X. B., Teng, J. W., Kong, X. R., et al. (2010). Crustal deformation of the eastern Tibetan plateau revealed by magnetotelluric imaging. *Nature Geoscience*, *3*(5), 358–362. https://doi.org/10.1038/NGEO830

Bai, L., Tian, X. B., & Ritsema, J. (2010). Crustal structure beneath the Indochina Peninsula from teleseismic receiver functions. *Geophysical Research Letters*, *37*(24), 701–719. https://doi.org/10.1029/2010gl044874

Bao, X., Song, X., Eaton, D. W., Xu, Y., & Chen, H. (2020). Episodic lithospheric deformation in eastern Tibet inferred from seismic anisotropy. *Geophysical Research Letters*, *47*(3), e2019GL085721. https://doi.org/10.1029/2019gl085721

Bao, X. W., Sun, X. X., Xu, M. J., Eaton, D. W., Song, X. D., Wang, L. S., et al. (2015). Two crustal low-velocity channels beneath SE Tibet revealed by joint inversion of Rayleigh wave dispersion and receiver functions. *Earth and Planetary Science Letters*, *415*, 16–24. https://doi.org/10.1016/j.epsl.2015.01.020

Bao, X. Y., Sandvol, E., Chen, Y. S. J., Ni, J., Hearn, T., & Shen, Y. (2012). Azimuthal anisotropy of Lg attenuation in eastern Tibetan Plateau. *Journal of Geophysical Research*, *117*, B10309. https://doi.org/10.1029/2012jb009255

Beaumont, C., Jamieson, R. A., Nguyen, M. H., & Medvedev, S. (2004). Crustal channel flows: 1. Numerical models with applications to the tectonics of the Himalayan-Tibetan orogen. *Journal of Geophysical Research*, *109*, B06406. https://doi.org/10.1029/2003jb002809

Boyd, O. S., Jones, C. H., & Sheehan, A. F. (2004). Foundering lithosphere imaged beneath the southern Sierra Nevada, California, USA. *Science*, *305*(5684), 660–662. https://doi.org/10.1126/science.1099181

Chen, H. P., Zhu, L. B., & Su, Y. J. (2016). Low velocity crustal flow and crust-mantle coupling mechanism in Yunnan, SE Tibet, revealed by 3D S-wave velocity and azimuthal anisotropy. *Tectonophysics*, *685*, 8–20. https://doi.org/10.1016/j.tecto.2016.07.007

Chen, L., Song, X., Gerya, T. V., Xu, T., & Chen, Y. (2019). Crustal melting beneath orogenic plateaus: Insights from 3-D thermo-mechanical modeling. *Tectonophysics*, *761*, 1–15. https://doi.org/10.1016/j.tecto.2019.03.014

Chen, M., Huang, H., Yao, H. J., van der Hilst, R., & Niu, F. L. (2014). Low wave speed zones in the crust beneath SE Tibet revealed by ambient noise adjoint tomography. *Geophysical Research Letters*, *41*(2), 334–340. https://doi.org/10.1002/2013GL058476

Chen, Y., Xu, Y. G., Xu, T., Si, S. K., Liang, X. F., Tian, X. B., et al. (2015). Magmatic underplating and crustal growth in the Emeishan large igneous province, SW China, revealed by a passive seismic experiment. *Earth and Planetary Science Letters*, *432*, 103–114. https://doi.org/10.1016/j.epsl.2015.09.048

Clark, M. K., & Royden, L. H. (2000). Topographic ooze: Building the eastern margin of Tibet by lower crustal flow. *Geology*, *28*(8), 703–706. https://doi.org/10.1130/0091-7613(2000)28<703:Tobtem>2.0.Co;2

Fan, G. W., & Lay, T. (2003). Strong Lg attenuation in the Tibetan Plateau. *Bulletin of the Seismological Society of America*, *93*(5), 2264–2272. https://doi.org/10.1785/0120030052

Furumura, T., & Kennett, B. L. N. (1997). On the nature of regional seismic phases. 2. On the influence of structural barriers. *Geophysical Journal International*, *129*(2), 221–234. https://doi.org/10.1111/j.1365-246X.1997.tb01577.x

Gan, W. J., Zhang, P. Z., Shen, Z. K., Niu, Z. J., Wang, M., Wan, Y. G., et al. (2007). Present-day crustal motion within the Tibetan Plateau inferred from GPS measurements. *Journal of Geophysical Research*, *112*, B08416. https://doi.org/10.1029/2005jb004120

He, B., Xu, Y.-G., Chung, S.-L., Xiao, L., & Wang, Y. (2003). Sedimentary evidence for a rapid, kilometer-scale crustal doming prior to the eruption of the Emeishan flood basalts. *Earth and Planetary Science Letters*, *213*(3), 391–405. https://doi.org/10.1016/S0012-821X(03)00323-6

Hoke, G. D., Liu-Zeng, J., Hren, M. T., Wissink, G. K., & Garzione, C. N. (2014). Stable isotopes reveal high southeast Tibetan Plateau margin since the Paleogene. *Earth and Planetary Science Letters*, *394*, 270–278. https://doi.org/10.1016/j.epsl.2014.03.007

Huang, H., Yao, H. J., & van der Hilst, R. D. (2010). Radial anisotropy in the crust of SE Tibet and SW China from ambient noise interferometry. *Geophysical Research Letters*, *37*, L21310. https://doi.org/10.1029/2010gl044981

Huang, Z. C., Wang, L. S., Xu, M. J., Ding, Z. F., Wu, Y., Wang, P., et al. (2015). Teleseismic shear-wave splitting in SE Tibet: Insight into complex crust and upper-mantle deformation. *Earth and Planetary Science Letters*, *432*, 354–362. https://doi.org/10.1016/j.epsl.2015.10.027

Huchon, P., Lepichon, X., & Rangin, C. (1994). Indo-China Peninsula and the collision of India and Eurasia. *Geology*, *22*(1), 27–30. https://doi.org/10.1130/0091-7613(1994)022<0027:Ipatco>2.3.Co;2

Iwakuni, M., Kato, T., Takiguchi, H., Nakaegawa, T., & Satomura, M. (2004). Crustal deformation in Thailand and tectonics of Indochina Peninsula as seen from GPS observations. *Geophysical Research Letters*, *31*(11), 373–374. https://doi.org/10.1029/2004gl020347

Jamieson, R. A., Unsworth, M. J., Harris, N. B. W., Rosenberg, C. L., & Schulmann, K. (2011). Crustal melting and the flow of mountains. *Elements*, *7*(4), 253–260. https://doi.org/10.2113/gselements.7.4.253

Jiang, G. Z., Hu, S. B., Shi, Y. Z., Zhang, C., Wang, Z. T., & Hu, D. (2019). Terrestrial heat flow of continental China: Updated dataset and tectonic implications. *Tectonophysics*, *753*, 36–48. https://doi.org/10.1016/j.tecto.2019.01.006

Kennett, B. L. N., & Engdahl, E. R. (1991). Traveltimes for global earthquake location and phase identification. *Geophysical Journal International*, *105*(2), 429–465. https://doi.org/10.1111/j.1365-246X.1991.tb06724.x

Kreemer, C., Blewitt, G., & Klein, E. C. (2014). A geodetic plate motion and Global Strain Rate Model. *Geochemistry, Geophysics, Geosystems*, *15*(10), 3849–3889. https://doi.org/10.1002/2014gc005407

Laske, G., Masters, G., Ma, Z., & Pasyanos, M. (2013). *Update on CRUST1.0 – A 1-degree Global Model of Earth's Crust*. EGU General Assembly 2013, EGU2013-2658, 7–12 April, Vienna, Austria.

Li, S. Y., Currie, B. S., Rowley, D. B., & Ingalls, M. (2015). Cenozoic paleoaltimetry of the SE margin of the Tibetan Plateau: Constraints on the tectonic evolution of the region. *Earth and Planetary Science Letters*, *432*, 415–424. https://doi.org/10.1016/j.epsl.2015.09.044

Liu, Q. Y., van der Hilst, R. D., Li, Y., Yao, H. J., Chen, J. H., Guo, B., et al. (2014). Eastward expansion of the Tibetan Plateau by crustal flow and strain partitioning across faults. *Nature Geoscience*, *7*(5), 361–365. https://doi.org/10.1038/ngeo2130

Liu, Z., Tian, X. B., Chen, Y., Xu, T., Bai, Z. M., Liang, X. F., et al. (2017). Unusually thickened crust beneath the Emeishan large igneous province detected by virtual deep seismic sounding. *Tectonophysics*, *721*, 387–394. https://doi.org/10.1016/j.tecto.2017.10.009

Ma, H. S., Wang, S. Y., Pei, S. P., Liu, J., Hua, W., & Zhou, L. Q. (2007). Q₀ tomography of S wave attenuation in Sichuan-Yunnan and adjacent regions. *Chinese Journal of Geophysics*, *50*(2), 465–471. https://doi.org/10.1002/cjg2.1051

Morley, C. K. (2002). A tectonic model for the tertiary evolution of strike-slip faults and rift basins in SE Asia. *Tectonophysics*, *347*(4), 189–215. https://doi.org/10.1016/S0040-1951(02)00061-6

Owens, T. J., & Zandt, G. (1997). Implications of crustal property variations for models of Tibetan plateau evolution. *Nature*, *387*(6628), 37–43. https://doi.org/10.1038/387037a0

Paige, C. C., & Saunders, M. A. (1982). LSQR: An algorithm for sparse linear equations and sparse least squares. *ACM Transactions on Mathematical Software*, *8*(1), 43–71. https://doi.org/10.1145/355984.355989

Qiao, L., Yao, H. J., Lai, Y. C., Huang, B. S., & Zhang, P. (2018). Crustal structure of southwest China and northern Vietnam from ambient noise tomography: Implication for the large-scale material transport model in SE Tibet. *Tectonics*, *37*(5), 1492–1506. https://doi.org/10.1029/2018tc004957

Richards, M. A., Duncan, R. A., & Courtillot, V. E. (1989). Flood basalts and hot-spot tracks: plume heads and tails. *Science*, *246*(4926), 103–107. https://doi.org/10.1126/science.246.4926.103

Royden, L. H., Burchfiel, B. C., King, R. W., Wang, E., Chen, Z., Shen, F., & Liu, Y. (1997). Surface deformation and lower crustal flow in eastern Tibet. *Science*, *276*(5313), 788–790. https://doi.org/10.1126/science.276.5313.788

Royden, L. H., Burchfiel, B. C., & van der Hilst, R. D. (2008). The geological evolution of the Tibetan Plateau. *Science*, *321*(5892), 1054–1058. https://doi.org/10.1126/science.1155371

Sarker, G., & Abers, G. A. (1999). Lithospheric temperature estimates from seismic attenuation across range fronts in southern and central Eurasia. *Geology*, *27*(5), 427–430. https://doi.org/10.1130/0091-7613(1999)027<0427:Ltefsa>2.3.Co;2

Shearer, P. M. (2009). *Introduction to seismology*. 2nd ed. Cambridge, NY. Cambridge University Press.

Shen, Z. K., Lu, J. N., Wang, M., & Burgmann, R. (2005). Contemporary crustal deformation around the southeast borderland of the Tibetan Plateau. *Journal of Geophysical Research*, *110*, B11409. https://doi.org/10.1029/2004jb003421

Stork, A. L., Selby, N. D., Heyburn, R., & Searle, M. P. (2008). Accurate relative earthquake hypocenters reveal structure of the burma subduction zone. *Bulletin of the Seismological Society of America*, *98*(6), 2815–2827. https://doi.org/10.1785/0120080088

Street, R. L., Herrmann, R. B., & Nuttli, O. W. (1975). Spectral characteristics of the Lg wave generated by central United States earthquakes. *Geophysical Journal International*, *41*(1), 51–63. https://doi.org/10.1111/j.1365-246X.1975.tb05484.x

Sun, X. X., Bao, X. W., Xu, M. J., Eaton, D. W., Song, X. D., Wang, L. S., et al. (2014). Crustal structure beneath SE Tibet from joint analysis of receiver functions and Rayleigh wave dispersion. *Geophysical Research Letters*, *41*(5), 1479–1484. https://doi.org/10.1002/2014GL059269

Sun, Y., Niu, F. L., Liu, H. F., Chen, Y. L., & Liu, J. X. (2012). Crustal structure and deformation of the SE Tibetan plateau revealed by receiver function data. *Earth and Planetary Science Letters*, *349*, 186–197. https://doi.org/10.1016/j.epsl.2012.07.007

Tapponnier, P., Lacassin, R., Leloup, P. H., Scharer, U., Dalai, Z., HaiweiW., & Jiayou, Z. (1990). The Ailao Shan/Red River metamorphic belt: Tertiary left-lateral shear between Indochina and South China. *Nature*, *343*(6257), 431–437. https://doi.org/10.1038/343431a0

Wang, J.-H., Yin, A., Harrison, T. M., Grove, M., Zhang, Y.-Q., & Xie, G.-H. (2001). A tectonic model for Cenozoic igneous activities in the eastern Indo–Asian collision zone. *Earth and Planetary Science Letters*, *188*(1), 123–133. https://doi.org/10.1016/S0012-821X(01)00315-6

Wang, W. L., Wu, J. P., Fang, L. H., Lai, G. J., & Cai, Y. (2017). Crustal thickness and Poisson's ratio in southwest China based on data from dense seismic arrays. *Journal of Geophysical Research: Solid Earth*, *122*(9), 7219–7235. https://doi.org/10.1002/2017JB013978

Wang, W. M., Zhao, L. F., Li, J., & Yao, Z. X. (2008). Rupture process of the Ms 8.0 Wenchuan earthquake of Sichuan, China. *Chinese Journal of Geophysics*, *51*(5), 1403–1410.

Wei, W., Zhao, D. P., & Xu, J. D. (2013). P-wave anisotropic tomography in Southeast Tibet: New insight into the lower crustal flow and seismotectonics. *Physics of the Earth and Planetary Interiors*, *222*, 47–57. https://doi.org/10.1016/j.pepi.2013.07.002

Wei, Z., Kennett, B. L. N., & Zhao, L.-F. (2017). Lg-wave attenuation in the Australian crust. *Tectonophysics*, *717*, 413–424. https://doi.org/10.1016/j.tecto.2017.08.022

Wessel, P., Smith, W. H. F., Scharroo, R., Luis, J., & Wobbe, F. (2013). Generic mapping tools: Improved version released. *Eos, Transactions American Geophysical Union*, *94*(45), 409–410. https://doi.org/10.1002/2013eo450001

Wu, R. S., Wu, X. Y., & Xie, X. B. (2007). *Simulation of high-frequency wave propagation in complex crustal waveguides using generalized screen propagators*. In R. S. Wu & V. Maupin (Eds.), Advances in Geophysics, Vol 48: Advances in Wave Propagation in Heterogeneous Earth (Vol. 48, pp. 323–363). San Diego, CA. Elsevier Academic Press Inc.

Xie, J. (2002). Lg Q in the Eastern Tibetan Plateau. *Bulletin of the Seismological Society of America*, *92*(2), 871–876. https://doi.org/10.1785/0120010154

Xu, L. L., Rondenay, S., & van der Hilst, R. D. (2007). Structure of the crust beneath the southeastern Tibetan Plateau from teleseismic receiver functions. *Physics of the Earth and Planetary Interiors*, *165*(3–4), 176–193. https://doi.org/10.1016/j.pepi.2007.09.002

Xu, T., Zhang, Z. J., Liu, B. F., Chen, Y., Zhang, M. H., Tian, X. B., et al. (2015). Crustal velocity structure in the Emeishan large igneous province and evidence of the Permian mantle plume activity. *Science China Earth Sciences*, *58*(7), 1133–1147. https://doi.org/10.1007/s11430-015-5094-6

Xu, X., Wen, X., Zheng, R., Ma, W., Song, F., & Yu, G. (2003). Pattern of latest tectonic motion and its dynamics for active blocks in Sichuan-Yunnan region, China. *Science in China – Series D*, *46*, 210–226. https://doi.org/10.1360/03dz0017

Yao, H. J., van der Hilst, R. D., & Montagner, J. P. (2010). Heterogeneity and anisotropy of the lithosphere of SE Tibet from surface wave array tomography. *Journal of Geophysical Research*, *115*, B12307. https://doi.org/10.1029/2009jb007142

Yin, A., & Harrison, T. M. (2000). Geologic evolution of the Himalayan-Tibetan orogen. *Annual Review of Earth and Planetary Sciences*, *28*, 211–280. https://doi.org/10.1146/annurev.earth.28.1.211

Yu, Y., Gao, S. S., Liu, K. H., Yang, T., Xue, M., & Le, K. P. (2017). Mantle transition zone discontinuities beneath the Indochina Peninsula: Implications for slab subduction and mantle upwelling. *Geophysical Research Letters*, *44*(14), 7159–7167. https://doi.org/10.1002/2017GL073528

Zhang, K. L., Liang, S. M., & Gan, W. J. (2019). Crustal strain rates of southeastern Tibetan Plateau derived from GPS measurements and implications to lithospheric deformation of the Shan-Thai terrane. *Earth and Planetary Physics*, *3*(01), 47–54. https://doi.org/10.26464/epp2019005

Zhang, P. Z. (2013). A review on active tectonics and deep crustal processes of the Western Sichuan region, eastern margin of the Tibetan Plateau. *Tectonophysics*, *584*, 7–22. https://doi.org/10.1016/j.tecto.2012.02.021

Zhang, P. Z., Shen, Z., Wang, M., Gan, W. J., Burgmann, R., & Molnar, P. (2004). Continuous deformation of the Tibetan Plateau from global positioning system data. *Geology*, *32*(9), 809–812. https://doi.org/10.1130/G20554.1

Zhao, C. P., Ran, H., & Chen, K. H. (2006). Present-day magma chambers in Tengchong volcano area inferred from relative geothermal gradient. *Acta Petrologica Sinica*, *22*(6), 1517–1528.

Zhao, L., Luo, Y., Liu, T. Y., & Luo, Y. J. (2013). Earthquake focal mechanisms in yunnan and their inference on the regional stress field. *Bulletin of the Seismological Society of America*, *103*(4), 2498–2507. https://doi.org/10.1785/0120120309

Zhao, L. F., & Mousavi, S. M. (2018). Lateral variation of crustal Lg attenuation in eastern North America. *Scientific Reports*, *8*(1), 7285. https://doi.org/10.1038/s41598-018-25649-5

Zhao, L. F., & Xie, X. B. (2016). Strong Lg-wave attenuation in the Middle East continental collision orogenic belt. *Tectonophysics*, *674*, 135–146. https://doi.org/10.1016/j.tecto.2016.02.025

Zhao, L. F., Xie, X. B., He, J. K., Tian, X. B., & Yao, Z. X. (2013). Crustal flow pattern beneath the Tibetan Plateau constrained by regional Lg-wave Q tomography. *Earth and Planetary Science Letters*, *383*, 113–122. https://doi.org/10.1016/j.epsl.2013.09.038

Zhao, L. F., Xie, X. B., Wang, W. M., Zhang, J. H., & Yao, Z. X. (2010). Seismic Lg-wave Q tomography in and around Northeast China. *Journal of Geophysical Research*, *115*(B08), 307. https://doi.org/10.1029/2009jb007157

Zhao, L. F., Xie, X. B., Wang, W. M., Zhang, J. H., & Yao, Z. X. (2013). Crustal Lg attenuation within the North China Craton and its surrounding regions. *Geophysical Journal International*, *195*(1), 513–531. https://doi.org/10.1093/gji/ggt235

Zheng, G., Wang, H., Wright, T. J., Lou, Y., Zhang, R., Zhang, W., et al. (2017). Crustal deformation in the India-Eurasia collision zone from 25 years of GPS measurements. *Journal of Geophysical Research: Solid Earth*, *122*(11), 9290–9312. https://doi.org/10.1002/2017jb014465

Zheng, T., He, Y., Ding, L., Jiang, M., Ai, Y., Mon, C. T., et al. (2020). Direct structural evidence of Indian continental subduction beneath Myanmar. *Nature Communications*, *11*(1), 1944. https://doi.org/10.1038/s41467-020-15746-3

Zhou, L. Q., Zhao, C. P., Xiu, J. G., & Chen, Z. L. (2008). Tomography of Q(Lg) in Sichuan-Yunnan zone. *Chinese Journal of Geophysics-Chinese Edition*, *51*(6), 1745–1752. https://doi.org/10.1002/cjg2.1312

Zhu, H. J., Bozdag, E., Duffy, T. S., & Tromp, J. (2013). Seismic attenuation beneath Europe and the North Atlantic: Implications for water in the mantle. *Earth and Planetary Science Letters*, *381*, 1–11. https://doi.org/10.1016/j.epsl.2013.08.030